Optical Beam Gradient Sensor

N. Müller, R. Lüning and F. Fleischmann
City University of Applied Sciences Bremen, Neustadtswall 30, 28199 Bremen, Germany
Email: friedrich.fleischmann@hs-bremen.de

Abstract

Freeform surfaces in optical components and local modifications of refractive index offer new degrees of freedom in the design of optical systems, resulting in smaller and lighter systems and increased performance. The measurement technique of experimental raytracing (ERT), based on deflectometry [1], has proven to be a suitable optical measurement technique to characterize topography as well as optical properties. In ERT, precise measurement of the gradient of small light beams is crucial for determination of these parameters. This usually includes the measurement of the position of the reflected ray in at least two parallel planes.
In this contribution, a new concept of an integrated beam inclination sensor [7] is introduced. It is retrieving gradient data of an incoming beam by measurement in one plane only, thus saving 50% measuring time. Theory, simulation and design of the sensor are presented as well as the strategy for signal evaluation in case of highly overlapping spots. Evaluation of a demonstrator device shows the high potential of the approach.

Keywords: Gradient sensor, Optical Measuring System, Deflectometry, Optical Freeform, Form Measurement, GRIN Lens, Gaussian mixture model.

1 Introduction

1.1 Motivation

While traditional spherical optical elements have been challenged by aspherical ones in the last years, advantages in manufacturing technology allows for even more beneficial non-rotational shapes [2]. Such freeform surfaces in optical components offer new degrees of freedom in the design of optical systems, resulting in smaller and lighter systems by increased performance [3]. This is also very helpful in technologies like head worn displays [4]. Freeform surfaces can be also used to create special illumination patterns [5,6]. Therefore, metrology is needed that is able to verify the surface form and quality [15, 16].
The next step are freeform gradient-index (F-GRIN) media. GRIN lenses show an additional potential for optical system performance by variation of the refractive index within the lens material. Metrology of such optical elements is still in an early state of development [7].
In either case, the measurement technique of experimental raytracing (ERT), based on deflectometry, [1] has proven to be a suitable optical measurement technique to characterize optical properties [8-12] like modulation transfer function (MTF), power map and surface retrieval from transmission test as well as for topography measurement of specular freeform surfaces [13, 14]. Drawback is the comparatively long measurement time required due to the necessary second scan for gradient measurement. The proposed new gradient sensor overcomes this limitation by giving gradient data in one single scan.

1.2 Theoretical background

The principle of ERT is based on scanning the aperture of a specimen with a test beam, detecting its change in direction after passing the device. The principle can be applied in reflection as well as in transmission, **figure 1** shows a typical configuration for testing aspherical lenses in transmission.
The source of the ray typically is a monochromatic laser.
The direction of the i-th ray after passing the test object is obtained by detecting its intensity distribution at detector positions $z_0,...,z_k$, $k > 0$, along the z-axis by an conventional image sensor. The coordinates of the intersect positions S^k_i are calculated from the captured images as center of mass of intensity distribution at sensor.

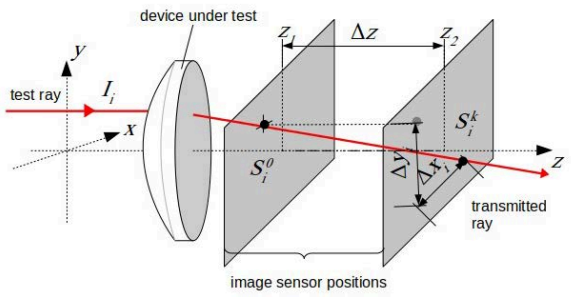

Figure 1: Schematic representation of the principle of experimental ray tracing.

For example, measuring the lateral displacement Δx, Δy of a ray I_i between two planes at z_2 and z_1 with distance

$\Delta z = z_2 - z_1$ as shown in **figure 1**, the slopes can be derived by

$$T_{i,x}=\frac{\Delta x_i}{\Delta z}, T_{i,y}=\frac{\Delta y_i}{\Delta z}$$

Over the eikonal, the rays are connected to the wavefronts by its gradient, so the wavefronts can reconstructed by appropriate methods [8]. From wavefront information, the optical parameters as well as surface shape can be derived.

A disadvantage of the ERT implementation used so far is that a measurement must be carried out at a minimum of two different positions, so a linear motion of the detector is necessary for each sample point i.

Using the gradient sensor proposed here, all the required data is determined with a single measurement and a repositioning to another position is obsolete. Furthermore, there is no need for sophisticated adjustments in meaning of setting a precise reference point of the sensor regarding z-position, as the measurement principle always refers to the first spot in trace.

2 Method

2.1 Principle

The sensor is constructed using an optically non-opaque material with a thickness h in between two partially reflecting mirrors with reflection coefficients R_1 and R_2, thus forming an etalon, in front of a CMOS-sensor [15]. A light beam, represented by a ray I_i, with incident angle γ_1 is refracted into the transparent material of the etalon following Snell's law, as depicted in **figure 2**.

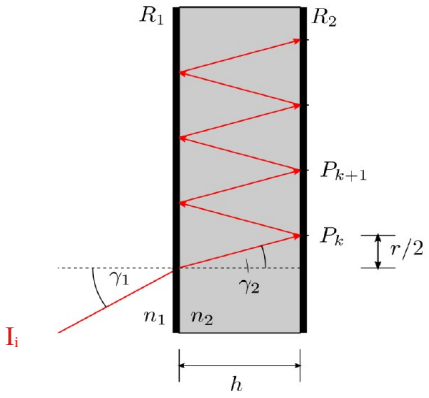

Figure 2: Schematic representation of the working principle using a non-opaque optical material with a refractive index n_2 between two partially reflecting coatings. The incident ray (red) is refracted into the beam splitter and is constantly reflected back and forth. P_k are indicating the position of reflection towards sensing element.

The refracted angle γ_2 and the thickness of the sensor h cause a lateral shift of the beam incident location at the second reflective layer towards the initial incident position at entrance into the beam splitter. The beam is reflected in between the reflective surface multiple times forming a trail of spots P_k at both surfaces while maintaining a constant spot distance r. The orientation of the spot trail indicates the rotational angle φ of the incident beam. The trail is observed by a CMOS Sensor placed in direction of second layer. In the situation depicted in **figure 3,** Sensor is placed on top (positive z-direction) of the sketched assembly.

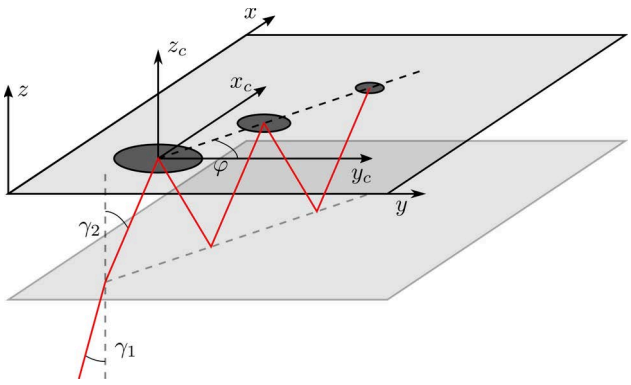

Figure 3: Schematic representation of the virtual ray path. Observing camera on top of sketched assembly.

Evaluating the spot trail, one gets incident angle γ_1 as

$$\gamma_1=\arcsin\left(\frac{n_2}{n_1}\cdot\sin\left(\arctan\left(\frac{r}{2h}\right)\right)\right) \quad (1)$$

with r denoting the (ideally) constant distance between spot positions P_k. Since refractive index is depending from wavelength, this has to be considered for high accuracy measurements. In case of an air spaced etalon in air, thus $n_1 = n_2 = 1$, γ_1 and γ_2 are identical and the relationship simplifies to

$$\gamma_1=\arctan\left(\frac{r}{2h}\right). \quad (2)$$

Assuming parallel reflection planes, positions P_k are on a straight line, and azimuthal angle φ can be derived from slope between first and second spot as

$$\phi=\arctan\left(\frac{\Delta y_P}{\Delta x_P}\right). \quad (3)$$

In the following, presentation focuses on the solid etalon type.

2.2 Limitations

The estimation of the incidence angle will be limited mostly by the uncertainty in spot distance r and thickness h. In reality, spots are represented by an intensity distribution that has neither sharp boundaries nor it is of ideal circular shape.

Since for any light beam represented by a ray using the paraxial approximation, the centre of mass of the beam's power density distribution (the spot) travels along this ray, and the calculation of centroids of the detected intensity distribution may be used to determine the direction of the ray from spot positions on sensor image. This works well as long as spots do not overlap each other or

ISBN 978-3-8007-5835-7

are cropped by sensor edges. As a first approach, beam is modelled as circular with a definite diameter d_{beam}. Using this, spots are separable if the spot distance is equal or bigger than the diameter of the beam, as sketched in **figure 4**.

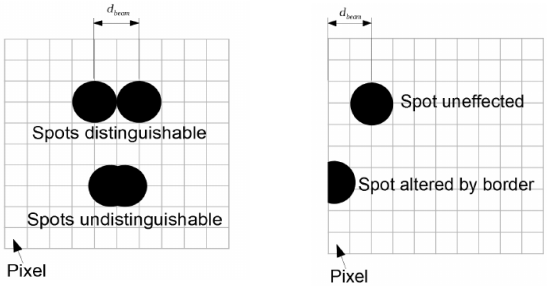

Figure 4: Sketch for the definition of distinguishable and undistinguishable spots (left) and edge effects (right).

From this, with L denoting the length of the detector, the minimal and maximum detectable inclination angles are given by

$$\gamma_{min} = \arcsin\left(\frac{n \cdot \frac{d_{beam}}{h}}{\sqrt{4 + \left(\frac{d_{beam}}{h} \right)^2}} \right), \tag{4}$$

and

$$\gamma_{max} = \arcsin\left(\frac{n \cdot \frac{L - 2\,d_{beam}}{h}}{\sqrt{4 + \left(\frac{L - 2\,d_{beam}}{h} \right)^2}} \right). \tag{5}$$

While these equations are describing the principle, for refined evaluation a more sophisticated model has to be used.

3 Simulation

3.1 Mathematical description

3.1.1 Image generation

The simulation of the sensor is derived by terms of geometric optics in paraxial approximation, applying the geometric properties for the basic TEM_{00} Gaussian base mode. Typical wave optics properties like divergence are neglected. For a given incoming ray I_i with inclination angle γ_1 and azimuthal angle φ, theoretical spot positions P_k are calculated from eq. (1) and (3). With beam width given as w_x and w_y in major axes of elliptical beam profiles and intensity I_k of k^{th} spot, a simulated image U according to the specified imaging sensor size is calculated by superposing K discrete Gaussian profiles with centers at the calculated spot locations (x_k; y_k) as

$$U(X', Y') = \sum_{k=1}^{K} I_k \exp\left(-2 \left(\frac{(X' - x_k)^2}{{w_x}^2} + \frac{(Y' - y_k)^2}{{w_y}^2} \right) \right) \tag{6}$$

X' and Y' describe the meshgrid representation of sensor pixel grid. No noise was added.
For reconstruction of γ_1 and φ, different clustering algorithms were evaluated.

3.1.2 Contour method

In contour finding approach, spots were identified after some basic image processing like dark image subtraction, thresholding and blurring. For contour finding, OpenCV `cv2.findContours` was used. For each detected spot, image was masked with spot's contour and centroid inside contour was calculated by `cv2.moment`.Repeating this for all detected spots, all centroid positions and distances between are derived and inclination as well as azimuthal angle are calculated.

3.1.3 Clustering

The spot detection on sensor image can be interpreted as a clustering task, with each illuminated pixel as an instance of a certain spot. Since clustering algorithms in image processing usually don't work on grey levels, but histogram data, the image grey value is converted to the number of occurrences at the respective pixel coordinate in a preprocessing procedure.
In case of fully separated spots (clusters), hard clustering algorithms like k-means are appropriate, but in spot detection for overlapping spots more probabilistic approaches are required.

3.1.3.1 Gaussian mixture model (GMM)

A GMM represents normal distributed sub-populations within an multimodal population. Due to the gaussian shape of the beam's intensity distribution it is a suitable model for overlapping spots. It superposes a number K of density functions, each describing a spot in sensor image with mixture ratio π_k, so that the probability mass function of data point x is given by

$$p(x|\theta) = \sum_{k=1}^{K} \pi_k \, \mathrm{N}(x|\mu_k, \Sigma_k) \tag{7}$$

with θ denoting a vector containing the component's mean μ_k and covariance matrix Σ_k for k = 1, 2, . . . , K. For angle determination, identification of the component's means is necessary. Since the estimation problem given in eq. 7 also contains latent variables, the parameter optimization is therefore performed using the expectation maximization algorithm" In estimation, advantage from properties of (ideal) etalon sensor properties can be taken. The implemented method is referenced to in this contribution as "modified GMM/EM":
Spots will always be equidistantly placed on a line, adding a condition for mean μ, representing spot distance. Each adjacent spot is a reflection of the previous spot, so only one covariance matrix Σ describes all spots. Since reflectance is known, the mixture ratios π_k of the components can be calculated and therefore be neglected in the optimization process.

3.1.3.2 Artificial Bee Colony (ABC)

EM algorithm is prone to convergence to local maxima. Here, the more recently popular ABC algorithm from the family of swarm optimization is used to determine the optimal set of parameters of the described Gaussian mixture model [16-18]. The ABC requires that a parameter vector which is to be optimized is parametrized. For etalon sensor this is simple for the mean μ and spot distance Δμ, which can be parametrized using the corresponding spatial components μ_x , μ_y , $\Delta\mu_x$ and $\Delta\mu_y$.
Parametrizing the covariance matrix has to ensure a positive semi-definiteness of the estimated variance covariance matrix. Implementing the approach of [19] finally leads to a seven-dimensional optimization problem.

3.1.4 Eigenvector method

The general shape and propagation direction can be estimated using the eigenvectors of the complete spot trail. The Eigenvector corresponding to the larger Eigenvalue is used for the estimation of the initial spot distance (and also for the estimation of the azimuthal angle). The smaller eigenvector can be used to estimate the initial covariance matrix.

3.2 Evaluation

3.2.1 Azimuthal angle

3.2.1.1 Test cases

Simulations used parameters close to the experimental setup, so a circular beam profile with fixed beam width of w = 200 μm was used.
Four typical test cases were defined:

1. separated spots (d = 4w, approx. 6° inclination).
2. slight overlap (d = 2w, approx. 3° inclination).
3. begin of complete overlap (2 points of inflection, unimodal distribution, d = 0.71w, approx. 1°).
4. typical overlap (half distance of 3, d=0.355w).

For each of the cases, the azimuthal angle was varied from 0° to 45° in steps of 0,5°. To determine the direction of the spot trail following methods were applied:

- centroid estimation by
  - state of the art contour finding method.
  - modified GMM/EM.
- spot trail from slope between the highest grey valued pixel and the centre of mass of the complete spot trail.
- Eigenvectors of the spot trail as described in 3.1.4, on a randomly subsampled dataset
- Eigenvectors on the complete dataset.

For implementation of GMM/EM, python library sklearn.mixture was used.

3.2.1.2 Results

In no cases a dependency on the rotational angle itself was observed, so the rectangular pixelgrid has no impact.

The investigations show an increase in error with decreasing incident angles for all investigated methods. As expected, the contour method yields excellent results for the larger investigated incident angles, but fails to detect spots for non-separable spots like for the two smaller incident angle cases. Spot trail from slope showed significant higher deviations than other methods, mainly due to the choice of highest pixel value instead of centroid. The Eigenvector approach with subsampling (10^5 samples) and the modified GMM/EM approach show similar results for all incident angles. The random subsampled dataset, which is incorporated in both approaches, results in rather dynamic deviations. The Eigenvector method on the complete dataset shows the lowest deviations from the set angle and is preferable over the subsampled approach, since savings in computation time are not significant. Nevertheless, none of the methods showed a systematic deviation.

3.2.2 Inclination angle

For investigation a set of artificial images using various incident angles with a fixed rotational angle φ = 0° were simulated, using the numerical framework described in Section 3.1. The inclination angle were increased in steps of 0.1° from γ_I = 0°, ... 6°. Each image was evaluated with following methods:

- contour method.
- standard GMM optimized with the classical EM
  - single initialization phase.
  - 10 times random initialization.
- modified GMM/EM algorithm.
- GMM + swarm optimization using ABC.

For GMM, 50 iterations were used. This process is repeated for ten iterations.

3.2.2.1 Results

From simulation, one can see that contour method works correctly for angle above 3.5°, standard GMM with 1 initialization run gives erroneous results in whole region, with 10 runs it performs well down to 1.2°.

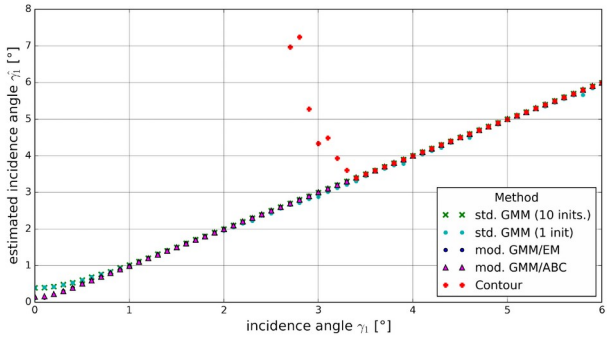

Figure 5: Comparison between the five incident angle estimation algorithms.

Modified GMM and mod. GMM with ABC work sufficiently from 0.2° on. A graphical representation is given in **figure 5**.

4 Experiment

4.1 Sensor design

Sensor was constructed on basis of Photonfocus BL1-D2080-160-G2 camera with Photonfocus A2080 CMOS sensor. As etalon, a Laseroptik beam splitter plate from fused silica, 20 mm × 20 mm, 6 mm thickness was used, reflectivity of coating 90 % (±1.5 %) at 532 nm. As depicted in **figure 6,** the etalon was tightly pressed directly on top of sensing element by 3D-printed holder, reducing gap c as far as possible. No index-matching fluid was used. Realized assembly is shown in **figure 7**.

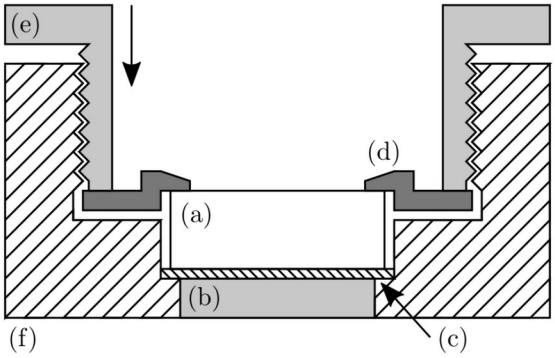

Figure 6: Construction of the etalon sensor based on Photonfocus BL1-D2020-160-G2. Beam splitter plate (a) on sensor element (b) with gap (c). Mounting of the etalon with screw mount (d,e) in the M42 camera body (f).

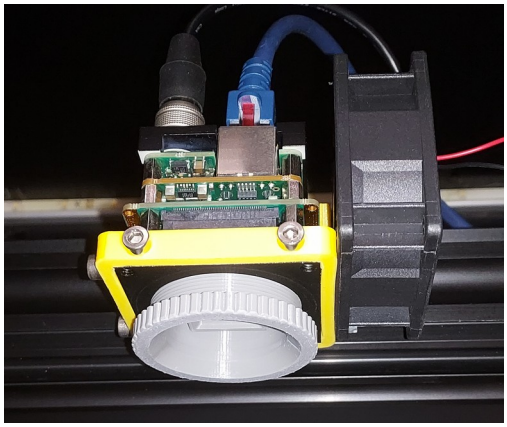

Figure 7: Realised Etalonsensor.

4.2 Setup

For evaluation, the setup depicted in **figure 8** was used. The sensor assembly was placed above a PI hexapod platform H-840.G1, which was used for controlling incident gradient by moving a collimated fibre LED mounted on top of the moving platform. The direction of the light beam can be altered in terms of rotation and incidence by moving the six DOF hexapod platform. Center of Etalonsensor was aligned to z-axis of hexapod platform, sensor plane parallel to hexapod platform.

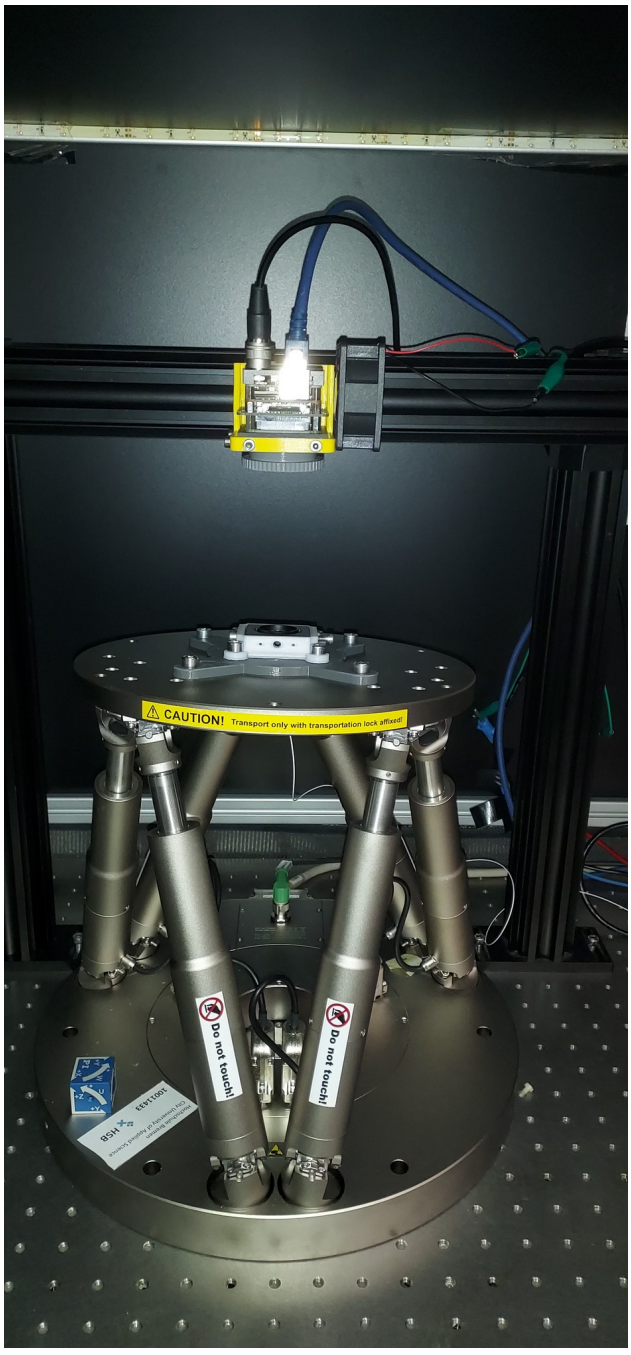

Figure 8: Measurement setup. Collimated fibre-coupled LED is placed on top of the moving platform of hexapod system PI H-840.G1.

4.3 Method

As a prerequisite, an estimation of the beam width was done. For an arbitrary incident angle, large enough with no spot overlapping, the Full Width at Half Maximum (FWHM) beam width was estimated from the first spot of the trail. For the investigated spot, a beam width of w = 208.59 µm was determined.

Each acquired image was pre-processed using a low pass filter with a Gaussian kernel of size 3 × 3 to reduce high frequency noise. In addition, a blacklevel offset of 4 % was applied, reducing the background illumination while

ISBN 978-3-8007-5835-7

retaining the Gaussian bell shapes of the spots. Therefore, all the illuminated spots are separated from the background. The number of spots is determined by counting the number of present spot using contour method, as long as no spots overlap.

4.4 Azimuthal angle

For measurement of azimuth angle estimation accuracy, the 4 testcases explained in section 3.2.1.1 are used, but adapted to the estimated beamwidth to $\gamma_1 = \{5.588°, 2.790°, 0.990°, 0.495°\}$. The procedure corresponds to simulation, but azimuthal angle was increased in steps of 1.0°. Evaluation of acquired and preprocessed images was identical to simulation.

4.5 Inclination angle

The measurement of inclination angle was realised exactly as in simulation. The direction of the incident light beam is altered by an automatic positioning of the hexapod platform. For each incident angle a total number of 10 images were acquired and individually evaluated.

5 Results

5.1 Azimuthal angle

Retrieved images for the 4 cases are given exemplarily in **figure 9**, deviations from set angle are shown in **figure 10**. Retrieved azimuthal angle in all cases show slight deviations from set angle.

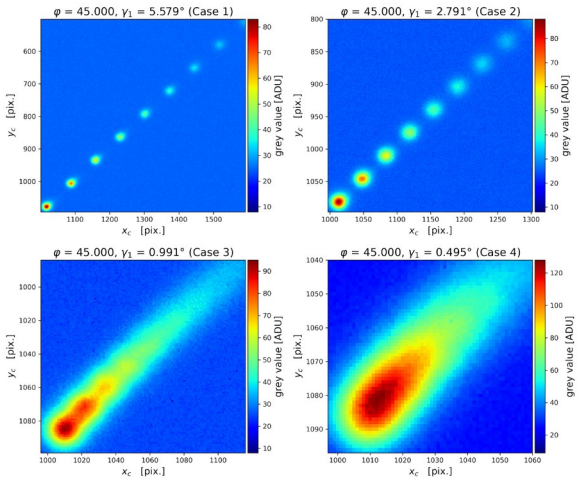

Figure 9: Exemplary images from measurement at fixed rotational angles φ = 45◦ for the four different incident angle cases.

Interestingly, both GMM methods show larger offset and variance values compared to the Eigenvector and contour finding approach. This behaviour differs from the expected similar performance of all methods shown in simulation. In cases 1 and 2 contour and Eigenvector method closely follow same trend in spite of different methodology, so underlying effects might be supposed.

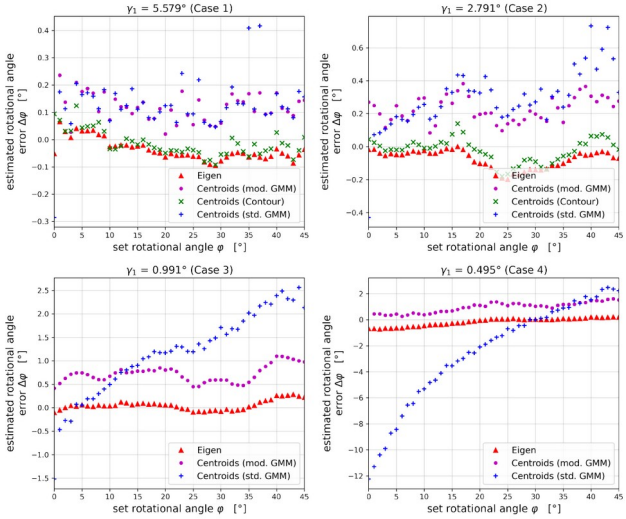

Figure 10: Comparison of azimuthal angle estimation error.

5.2 Inclination angle

The contour finding method returns the incident angle very precisely and reliably with barely any fluctuations for large incident angles down to incident angles of 2°. Both the modified GMM/EM, as well as the GMM/ABC approach are able to return the most accurate incident angles throughout the complete measurement range with barely any fluctuations, the classic GMM however shows significant fluctuations, see **figure 11**.

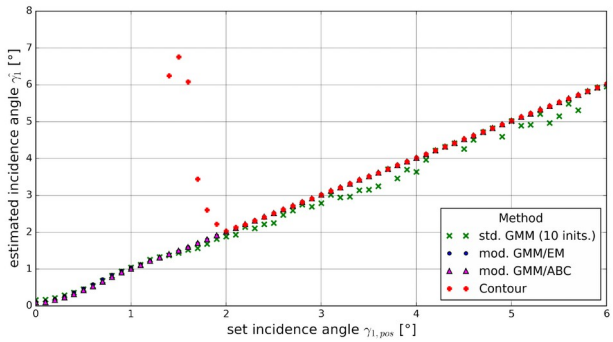

Figure 11: Deviation of measured inclination versus set angle.

To summarize, the Eigenvector method outperforms all other methods in retrieval of azimuthal angle at small incident angles, while modified GMM/EM is superior in retrieval of incident angle, working down to 0.2° correctly.

6 Conclusion

For measurement of large incident angles exceeding 6°, the simple contour finding method promises the most accurate results alongside with the Eigenvector method presented here.
Even in case of highly overlapping spots, in this realization at inclination angles smaller approx. 3°, evaluation

methods were proposed achieving highly correct estimation of inclination and azimuthal angle down to inclination angles of 1.0°. In region 0,2° - 1.0°, deviations in inclination angle estimation of max. 0.05° were present. With modified thickness and reflection coefficients the measurement range can be optimized for a given situation.
Further work has to be done to investigate sources of offset error in azimuthal estimation, especially in the region at 25°-30°. This is likely due to internal realization of pixelgrid and trenches. Also, homogeneity of angle estimation over complete sensor element has to be evaluated and influence of misaligned beamsplitters must be investigated.

In total, the gradient sensor has proven to be a reliable device for measurement of inclination and rotation of incident light beams even at small inclination angles.

7 Acknowledgement

We gratefully acknowledge financial support through the Federal Ministry for Economic Affairs and Energy (BMWi), WiPaNo-program, Grant No. 03THW04L06.

8 Literature

[1] Häusler, G. and Schneider, G.: Experimental ray tracing with a lateral effect photodiode.
Appl. Opt., 27 (1988) 5160-5164.

[2] K. P. Thompson and J. P. Rolland: Freeform optical surfaces: a revolution in imaging optical design. Opt. Photon. News 23, 30–35, 2012.

[3] K. Fuerschbach, J. P. Rolland, and K. P. Thompson: A new family of optical systems employing phi-polynomial surfaces.
Opt. Express 19, 21919-21928 (2011)
https://doi.org/10.1364/OE.19.021919

[4] O. Cakmakci, S. Vo, S. Vogl, R. Spindelbalker, F. A. and J. P. Rolland: Optical free-form surfaces in off-axis head-worn display design.
7th IEEE/ACM International Symposium on Mixed and Augmented Reality, pp. 29-32, 2008.
https://doi.org/10.1109/ISMAR.2008.4637320

[5] M. Essameldin et al.: Functional concept for the source independent beam-shaping of LED light.
OSA Continuum, Vol. 2 (2019) No. 3, 759-766.

[6] J. C. Minano, P. Benitez and A. Santamaria: Free-Form Optics for Illumination.
Optical review Vol. 16 (2009) No. 2, 99–102.

[7] David H. Lippman, et al.: Freeform gradient-index media: a new frontier in freeform optics.
Opt. Express **29**, 36997-37012 (2021)

[8] D. Hilbig et al.: Experimental ray tracing for characterization of optical components.
http://www.dgao-proceedings.de (2016) ISSN: 1614-8436

[9] T. Binkele et al.: Determination of the paraxial focal length of strong focusing lenses using Zernike polynomials in simulation and measurement.
Proc. of SPIE Vol. 9960 (2016).
https://doi.org/10.1117/12.2238059

[10] Ceyhan, U. et al.: Measurements of aberrations of aspherical lenses using experimental ray tracing.
Proc. SPIE 8082 (2011).
https://doi.org/10.1117/12.895009

[11] A. Alinoori et al.: Topography measurement of free-form specular surfaces using experimental ray tracing and radial basis functions.
Proc. SPIE 9961 (2016).
https://doi.org/10.1117/12.2237665

[12] G. Gutierrez, D. Hilbig, F. Fleischmann, T. Henning: Locally resolved characterization of progressive addition lenses by calculation of the modulation transfer function using experimental ray tracing,
Proc. SPIE 10110, 10110E (2017).
https://doi.org/10.1117/12.2251992

[13] Tobias Binkele et al.: Characterization of gradient index optical components using experimental ray tracing.
Proc. SPIE 10925, Photonic Instrumentation Engineering VI, 109250D (4 March 2019)
https://doi.org/10.1117/12.2511072

[14] Binkele, T. et al.: Characterization of specular free-form surfaces from reflected ray directions using experimental ray tracing.
J. Sens. Sens. Syst. 10 (2021), 261–270.
https://doi.org/10.5194/jsss-10-261-2021.

[15] T. Henning, F. Fleischmann: Vorrichtung und Verfahren zur optischen Analyse eines Prüflings.
German Patent application 102016209090 (2016).

[16] D. Karaboga: An idea based on honey bee swarm for numerical optimization, technical report - tr06,
Technical Report, Erciyes University, (01 2005)

[17] X. Xie, Y. Gao, W. Shi, and Q. Shen: Classification and detection of adulteration in olive oil using improved gaussian mixture model and regression by artificial bee colony algorithm.
Chemical Engineering Transactions, vol. 55, pp. 349–354 (2016)
https://www.cetjournal.it/index.php/cet/article/view/CET1655059

[18] A. E. Culos, J. L. Andrews, and H. Afshari: An artificial bee colony algorithm for mixture model-based clustering,
Communications in Statistics – Simulation and Computation, vol. 0 (2020) no. 0, pp. 1–12.
https://doi.org/10.1080/03610918.2020.1779291

[19] M. Lindstrom and D. Bates: Newton-raphson and em algorithms for linear mixed-effects models for repeated-measures data,
Journal of the American Statistical Association, vol. 83, pp. 1014–1022 (1988)